IOP Publishing and International Atomic Energy Agency Nuclear Fusion
Nucl. Fusion **52** (2012) 063005 (16pp) doi:10.1088/0029-5515/52/6/063005

Characterization of disruption halo currents in the National Spherical Torus Experiment

S.P. Gerhardt[1], J. Menard[1], S. Sabbagh[2] and F. Scotti[1]

[1] Princeton Plasma Physics Laboratory, Princeton, NJ 08543, USA
[2] Department of Applied Physics, Columbia University, New York, NY, 10027, USA

Received 22 November 2011, accepted for publication 22 March 2012
Published 17 April 2012
Online at stacks.iop.org/NF/52/063005

Abstract
This paper describes the general characteristics of disruption halo currents in the National Spherical Torus Experiment (Ono *et al* 2000 *Nucl. Fusion* **40** 557). The commonly observed types of vertical motion and resulting halo current patterns are described, and it is shown that plasma discharges developing between components can facilitate halo current flow. The halo current fractions and toroidal peaking factors at various locations in the device are presented. The maximum product of these two metrics for localized halo current measurements is always significantly less than the worst-case expectations from conventional aspect ratio tokamaks (which are typically written in terms of the total halo current). The halo current fraction and impulse is often largest in cases with the fastest plasma current quenches and highest quench rates. The effective duration of the halo current pulse is comparable to or shorter than the plasma current quench time. The largest halo currents have tended to occur in lower β and lower elongation plasmas. The sign of the poloidal halo current is reversed when the toroidal field direction is reversed.

(Some figures may appear in colour only in the online journal)

1. Introduction and background

Tokamak [1] discharges sometimes end in unplanned terminations known as disruptions [2, 3]. During these events, the plasma thermal energy is lost on a very short time-scale [2, 3], followed by a rapid decay of the plasma current in the resistive cold plasma [4–9]; these phases of the disruption are known as the thermal and current quench, respectively. The impulsive thermal loading associated with this energy loss [2, 3, 10–12] can lead to severe melting and/or ablation of material surfaces facing the plasma. The eddy currents driven by the current quench can cause large electromagnetic loads on in-vessel components [13]. Furthermore, it is possible for a large fraction of the pre-disruption plasma current to be converted to runaway electrons [2, 3, 14–20], which have the potential to cause severe localized damage to in-vessel components if they become deconfined [21].

It is the purpose of this paper, however, to study a fourth major disruption consequence: the phenomenon of 'halo currents' [2, 3, 22–40]. The tokamak concept generally optimizes towards large elongation of the plasma cross-section, essentially due to the additional safety factor that such plasma boundary shaping provides [41–44]. This elongated plasma shape implies that the discharge will be unstable to vertical motion [45, 46], and that feedback control of the vertical position is required [41, 46–48]. This vertical control can be lost, either during the otherwise steady portion of the discharge, or after the thermal quench of a disruption. In either case, the resulting vertical motion brings the plasma in contact with either the top or bottom of the vacuum chamber. Currents can then flow between the plasma and the in-vessel components. The poloidal component of these currents flowing in components, when crossing the strong tokamak toroidal field, can result in unacceptably large forces on those components. These halo currents are expected, for instance, to cause very large mechanical loading on components in the ITER tokamak [2, 3, 13, 49]. Note that we define 'halo current' to include any current that links both the plasma and conducting structures; this would include the 'Hiro current' of [34, 39].

Halo currents have been characterized in a large number of conventional tokamak devices, including ALCATOR C-Mod [28], ASDEX-Upgrade [30, 37, 38], COMPASS-D [29], DIII-D [4, 22, 23, 26, 36], JET [24, 31–33, 35] and JT-60U [27]. These devices have generally shown large halo currents, with worst-case events having up to 50% of the pre-disruption plasma currents flowing into the vessel and plasma facing components [2]. The halo currents are also observed to have structure in the toroidal direction, such that some toroidal angles will experience a concentration of the halo current load. In some cases, that structure has been observed to rotation

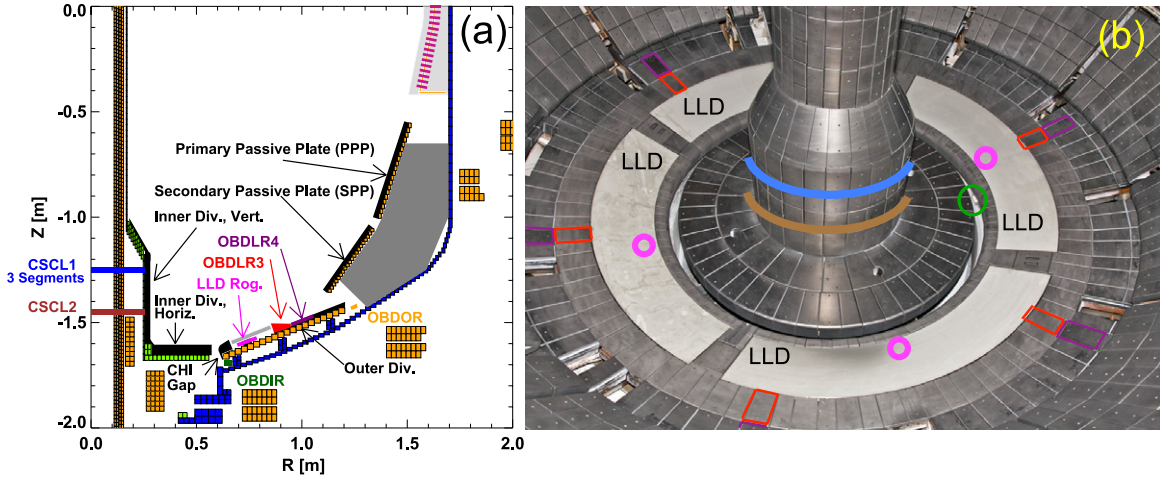

Figure 1. Layout of halo current diagnostics in NSTX. They are shown schematically in (*a*), along with labels for the various divertor sections and passive plates. (*b*) shows a photograph of the lower divertor, with diagnostics indicated with the same colour scheme as in (*a*). Note the green circle around the single visible inner-ring B_T detector in (*b*).

toroidally [28]. Given these results, it is important to note that the reduction in halo currents with 'massive gas injection' (MGI) [50–59] has been documented in ALCATOR C-Mod [53], DIII-D [51], JET [58], and ASDEX-Upgrade [56].

In contrast to this large database, halo currents have previously been assessed in only two spherical torii: limited measurements were performed in the small START device [60], and more extensive measurements have been made in the larger, $I_P = 1$ MA class, MAST device [61, 62]. Importantly, these results showed that the toroidal peaking of halo currents on the centre column, where the toroidal field is largest, was quite low. Reference [62] also described the tendency of the toroidal peaking factor to increase at larger major radius.

This paper studies the characteristics of halo currents in the National Spherical Torus Experiment (NSTX) [63]. This device is a medium sized spherical torus (ST), with major radius R_0 of 0.85 m and typical aspect ratios R_0/a of 1.35–1.6, designed to study the potential core plasma performance improvements associated with a reduced aspect ratio [64–69] (here, a is the minor radius). Plasmas are typically heated with up to 7 MW of neutral beams, or up to 6 MW of high-harmonic fast waves. The plasma is controlled with a flexible digital plasma control system, developed by General Atomics [70–72] and deployed on NSTX [73, 74]. The plasma shape and position are controlled using the Isoflux algorithm [75, 76], with an additional derivative control term on the vertical position outside that shape controller. However, vertical control can be lost after events such as previously rotating tearing modes that slow and lock to the wall [44, 77], or resistive wall modes [78, 79]; these 'vertical displacement events' (VDEs) will be referred to as 'inadvertent'. We also generate 'deliberate' VDEs by freezing the voltage on the radial field coils and allowing the plasma to drift in an uncontrolled manner (often with a 'kick' in order to force the direction of motion).

The rest of this paper is organized as follows. Section 2 provides a description of the halo current diagnostics and analysis techniques used in this paper. Example waveforms documenting the most common halo current patters detected in NSTX are shown in section 3. Database analysis of halo currents in provided in section 4. The effect of toroidal field reversal on the halo current direction is discussed in section 5. A summary and discussion are given in section 6.

2. NSTX device and halo current instrumentation

Many of the key electrical and structural features of NSTX are illustrated in figure 1. The NSTX vacuum vessel is made up of inner and outer vessels, where 'inner' refers to small major radius, and outer refers to large major radius. These vessel sections are isolated from each other by ceramic insulators. This allows 'coaxial helicity injection' (CHI) to be tested as a plasma startup method [80, 81]. The regions between the inner and outer vessels (at both the top and bottom of the machine) are referred to as the CHI gap.

Starting with the 2007 run campaign, NSTX has been outfitted with an expanding suite of halo current detectors. This instrumentation is described in great technical detail in [82], and will be described only briefly here. This halo current instrumentation, shown schematically in figure 1, can be divided into two different types: (i) instrumentation that measures current in the chamber walls, and (ii) instrumentation that measures the entrance and exit points of halo currents. The colour scheme indicating the various detectors in figure 1 will be used for all subsequent figures. Table 1 also provides a summary of the diagnostics.

The first type of sensor (wall current measurements) includes Rogowskis on the centre stack casing (CSC), which measure currents flowing vertically on the inconel tube that provides the inboard vacuum boundary for the device. There are two of these Rogowskis on the lower centre column (denoted CSCL1 and CSCL2), and one on the upper centre column (denoted CSCU2, and not visible in figure 1). The CSCL1 Rogowski has been divided toroidally into three segments, in order to infer the toroidal peaking of the halo currents.

The vessel wall current measurements also include two arrays of discrete B_T detectors mounted to the vacuum chamber wall and functioning like the sections of a partial Rogowski. There are six B_T detectors per array, with the sensors of

Table 1. Description of halo current instrumentation in NSTX.

Designation	Measurement type	Location	Type of halo current
CSCL1	Three segmentRogowski	Lower centre column	Poloidal current magnitude and toroidal peaking in the lower centre column
CSCL2	Continuous Rogowski	Lower centre column	Poloidal current magnitude in the lower centre column
CSCU1	Continuous Rogowski	Upper centre column	Poloidal current magnitude in the upper centre column
OBDLR3	Shunt tile	Lower outboard divertor, row-3 tiles	Magnitude and toroidal structure of current flowing into or out of divertor
OBDLR4	Shunt tile	Lower outboard divertor, row-4 tiles	Magnitude and toroidal structure of current flowing into or out of divertor
OBDIR	Local toroidal field	Inboard of outer divertor and outboard of CHI gap	Magnitude and peaking of current flowing in the lower vessel near the CHI gap.
OBDOR	Local toroidal field	Inboard/under lower secondary passive plates and outboard of lower outer divertor	Magnitude and peaking of current flowing in the lower vessel under the secondary passive plates.
CTCHILP	Pearson current transducer	Buswork connecting inner and outer vessels	Magnitude of current flowing from inner to outer vessel.
LLD Rog.	Small Rogowski	Under each LLD tray	Current flowing into or out of each LLD tray

each array located at the same poloidal angle, but toroidally separated by $\sim 60^\circ$. One of these arrays is located on the inboard side of the outer divertor, on the large major radius side of the CHI gap. The other is located just outside of the outer divertor, under/behind the lower secondary passive plates. These two arrays of detectors will be referred to below as the inner ring (OBDIR for outboard divertor, inner ring) and outer ring (OBDOR for outboard divertor, outer ring), respectively.

As is described in [82], the toroidal peaking factor derived directly from these magnetic measurements underestimates the true peaking of the halo currents. Essentially, the toroidal field produced by the poloidal halo currents is less toroidally peaked than the underlying poloidal currents. The measurements are explicitly of the toroidal field, and thus underestimate the peaking of the underlying current. Reference [82] provides approximate formulae for converting the measured (toroidal field) peaking factors to the halo current peaking factors. The segmented Rogowski peaking factors shown in this paper have been corrected using the cosine approximation in table 1 of [82], while the discrete B_T detector peaking factor has been corrected using the cosine approximations in table 2 of that same reference.

Although the outer and inner vessels are isolated from each other, they share a common single-point ground during non-CHI operations. The copper buswork runs that connect the vessel sections to the common single-point ground are instrumented with current transducers. The connection points are at the vessel bottom on either side of the CHI gap. Current is often detected on these sensors during a disruption, and the data from these transducers will be shown in some plots below; these will be denoted CTCHILP (for current transducer, coaxial helicity injection, lower, positive lead). Note that because it is a single-point ground, there is no net ground current: the current that flows in this buswork from the inner vessel always goes to the outer vessel, then return through the plasma.

The second type of detectors are those used to measure the entrance and exit points of the halo currents. The most important detectors in this group are 12 'shunt tiles', 6 each in two rows of the outboard divertor. These tiles are instrumented with resistive shunts between the tile and the divertor floor. The voltage on the shunt is used to infer the current flowing into or out of the given tile. The total current flowing into the given row of tiles can be estimated by multiplying the total current flowing to the six tiles by the ratio of the total row area to the area of the six instrumented tiles: $I_{\rm row} = (A_{\rm row}/6A_{\rm tile}) \sum_{i=1}^{6} I_{{\rm tile},i}$. The toroidal peaking factor can be easily determined as the instantaneous maximum of the 6 signals normalized to their mean. There are shunt tiles in rows 3 and 4 of the outboard divertor, which will be referred to as OBDLR3 and OBDLR4, respectively.

This second measurement type also includes special small Rogowski coils [83] mounted on the grounding posts of the liquid lithium divertor (LLD) trays. The LLD trays are molybdenum coated copper conic sections in the lower divertor, designed to test the response of the plasma to a thin liquid lithium film; see [84] for additional details regarding LLD. The LLD trays were designed to be single-point grounded, such that these Rogowskis would measure the total current flowing into a given plate. While the Rogowskis functioned as designed, other paths from the LLD plate to the vessel developed as the run campaign progressed; data from these instruments are only shown for examples early in the 2010 campaign. Also, the graphite tiles between the LLD trays (see figure 1(*b*)) are $\sim$1 cm proud of the LLD surface, and so presumably collect a larger share of the halo current than would be inferred from their toroidal extend alone. For these reasons, the current measured by these Rogowski coils is only a lower bound on the total halo current flowing at this poloidal location, and are only shown in select examples. Note also that the row of tiles directly inboard of the LLD is not instrumented for halo current detection.

In addition to the halo current measurements, this analysis will rely on reconstructions of the plasma equilibrium. When considering the 'typical' or flat-top average of quantities, we typically use the standard NSTX EFIT reconstructions available for nearly all discharges [78, 85]. These automatic reconstructions, however, are typically of insufficient time resolution to resolve the dynamics just proceeding the disruption. Hence, high time-resolution ($\delta t = 1$ ms) reconstructions up to the time of the large halo currents have been computed using the LRDFIT code [86]. These reconstructions are constrained by measurements of the

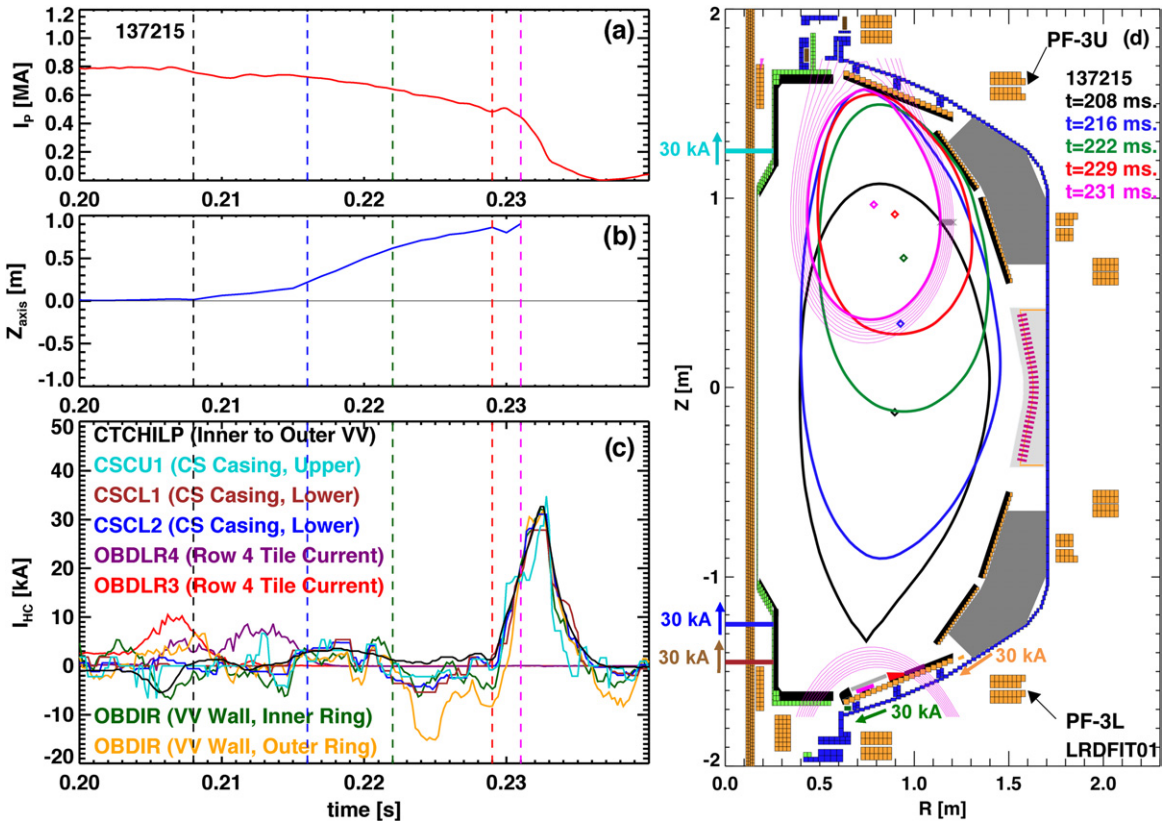

Figure 2. An example upward-going VDE. Shown are time traces of (*a*) the plasma current, (*b*) the plasma vertical position, (*c*) the various halo currents, and (*d*) five equilibria in the sequence leading to the disruption.

total plasma + vessel current [87], poloidal field and flux measurements around the plasma periphery, and the signal from a diamagnetic loop. This code does not at present have the ability to fit currents outside the last closed magnetic surface, and so is not used to reconstruct equilibria during the phase with strong halo currents.

3. Examples of halo current waveforms

Given the halo current detectors present in NSTX, there are three typical halo current patterns observed in NSTX; describing these patterns is the purpose of this section. The first pattern is for upward VDEs, where currents flowing around the lower part of the vessel are detected. The second pattern is for VDEs that land on the lower secondary passive plates. The third pattern is for VDEs that land on the lower outboard divertor. Examples from each of these three scenarios are described in detail below; we note that there are other halo current scenarios and flows that are not discussed here on account of the lack of measurements or their relative rarity.

3.1. Upward VDE

Example traces from the upward-going VDE 137215 are shown in figure 2. This discharge suffered an H $\rightarrow$ L transition just after the start of the I_P flat-top, when the neutral beam heating power was reduced from 4 to 2 MW at $t = 0.16$ s. A significant loss of stored energy and modification of the profiles followed, with the discharge developing strong vertical motion and ultimately impacting on the upper divertor. The final thermal and current quenches occur at $t = 0.228$ s. Frames (*a*), (*b*) and (*c*) show the evolution of the plasma current, the vertical position, and the halo currents, while frame (*d*) shows the plasma boundary evolution up to the point of strong halo currents. The vertical lines in the time traces indicated the times of the reconstructions, with the same colour code as in frame (*d*).

Given that nearly all of the halo current instrumentation is located in the vessel bottom, it might appear unlikely that currents would be measured for an upward-going VDE. However, the electrical break at the top of the machine (between the inner and outer vessels) implies that any current flowing out of the upper-inner divertor, around the plasma, and into the upper-outer divertor must return by flowing around the entire poloidal circumference of the vacuum chamber.

This can be clearly seen in figure 2, where a halo current transient of ~30 kA is observed in the OBDIR and OBDOR lower vessel wall current detectors. The same current transient is then observed to flow through the buswork connecting the inner and outer vessel, and then on all three centre-column Rogowskis. There are likely much larger currents flowing locally in the upper divertor structures, but these are not resolved with the present measurements.

The SOL poloidal flux contours are shown for the final viable reconstruction in frame (*d*); these contours are spaced by 1 cm at the outboard midplane side of the plasma (indicated by the black 'x's in the figure, where 'midplane' is defined by the point on the plasma boundary with the largest radial

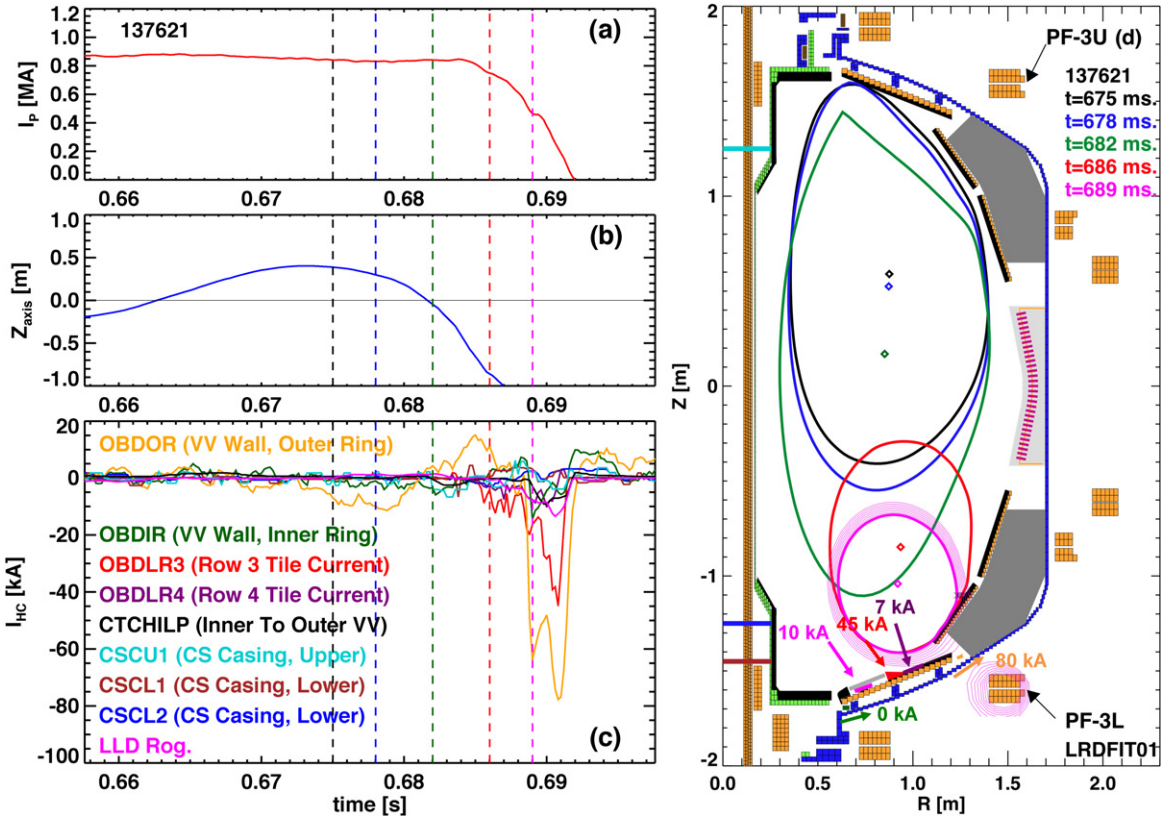

Figure 3. An example downward-going VDE that lands on the lower secondary passive plate. The individual frames contain the same data types as figure 2.

coordinate). The inboard divertor, out of which the observed halo currents must be flowing, is linked by the 4–5 cm flux lines, indicated that the width of the halo region is at least this wide.

We also note that the TF rod current is downwards in this case, making a clockwise toroidal field when viewed from above. Previous tokamaks [28, 29] and STs [62] have found that the centre-column currents are typically in the same direction as the rod current, such that they apply a compressive force on the PFCs and other current carrying components. The electrical break at the top of NSTX yields the opposite result for these upward disruption: the poloidal current is in the direction opposite the rod current, yielding a reversal in the direction of force. This result emphasizes the importance of details in the electrical configuration of the vessel in determining the halo current patterns and loads.

3.2. Downward VDE landing on the secondary passive plate

A second common pattern of halo currents occurs when the plasma impacts the low secondary passive plate in NSTX, as illustrated in the boundary traces of figure 3. In this case, a previously rotating $n = 1$ MHD perturbation locked to the vessel wall at $t = 0.646$. The locking and subsequent dynamics triggered a growing oscillation in the plasma vertical position. That the plasma first contacts the secondary passive plates is indicated by the fast framing visible light images in figure 4(*a*), where a band of strong interaction indicates contact with those plates starting at about $t = 0.685$ s. This interaction continues throughout the disruption phase (see figure 4(*b*)), indicating the continued interaction of the plasma with the secondary passive plate.

As indicated in figure 3, a peak current of ∼70 kA is observed in the outer-ring vessel wall detectors (OBDOR), flowing to larger major radius (i.e. towards the secondary passive plate). The majority of this current (∼45 kA) is observed to enter the outer divertor through the row-3 tiles (OBDLR3). Approximately 10 kA of this current is observed to enter the LLD trays, and as indicated in section 2, this number likely underestimates the total current flowing at that poloidal angle due to the proud gap tiles. Interestingly, comparatively little current enters the row-4 shunt tiles (OBDLR4) in this case. As indicated by the 1 cm spaced flux lines in the figure, it appears that the field lines have only grazing incidence with these tiles, such that very little current is collected by them in this instance. However, the row-3 tiles reside on the 5–8 cm flux lines, and do collect significant current.

3.3. Downward VDE landing on the outboard divertor

The final style of disruption under consideration is that which impacts directly on the lower outboard divertor; an example of this type is shown in figure 5. Once again, the plasma develops a vertical position oscillation, after which control is lost. Initially (at $t = 0.190$ s), up to 30 kA is observed to flow through the buswork connecting the inner and outer vessels, then along the lower vacuum vessel where it is detected

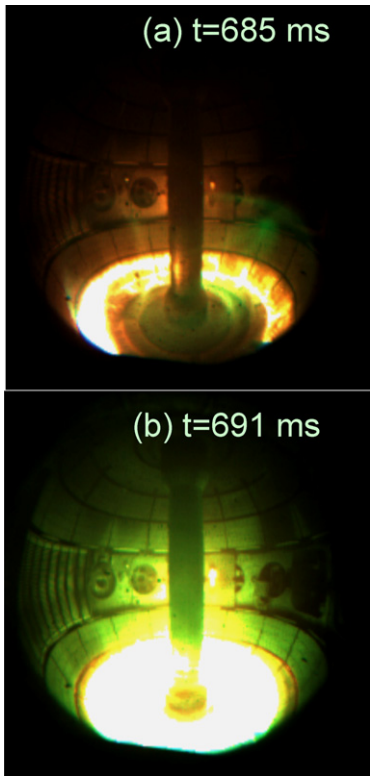

Figure 4. Visible light images of the plasma impacting the secondary passive plates during a VDE. (*a*) shows the plasma limiting on the secondary plates at $t = 0.685$ s, while (*b*) shows the plasma in the lower divertor in continued contact with the passive plates.

by the inner-ring detector array (OBDIR). This current is then observed to flow out of the LLD plates and shunt tiles. Reasonable reconstructions of the equilibria are available up to this time. From these measurements, we infer again that the halo width is at least ~8 cm when mapped to the plasma midplane.

This behaviour changes dramatically at ~190 ms, when the halo currents detected by the inner-ring detector array (OBDIR) increase dramatically, while the currents flowing via buswork from inner to outer vessel start to decrease. This behaviour can be understood by inspecting the images of the lower divertor in lithium I light in figure 6 (there was substantial lithium conditioning of the plasma facing components [88] in these cases, such that lithium light is a good indicator of low temperature plasma). At 189.6 ms (frame (*a*)), the CHI gap is visible as a dark band. This has begun to change at 190.6 ms, where a band of bright light is visible from the CHI gap. The light from this band has increased in intensity by 191.6 ms, where it is clear that plasma has filled the CHI gap region. This plasma completes the circuit from inner to outer divertor, allowing currents to bridge the CHI gap and flow from the inner to outer vessel without utilizing the connecting buswork.

At the time of peak halo current, there are approximately 70 kA of current flowing in the vessel wall near the CHI gap, the majority of which is likely conducted by the aforementioned plasma in the gap. An unknown, but likely large, amount of current flows into the divertor tiles just inboard of the LLD near the CHI gap. We observe approximately 50 kA of current flowing out of the row-3 tiles, and 25 kA flowing out of the row-4 tiles. At least 40 kA of current is observed to flow out of the LLD trays.

We also note that this case has a small amount of halo current detected in the centre-column Rogowskis. These sensors are in the far halo for this type geometry of disruption, and so are not expected to detect significant current. The direction of current is downwards, parallel to the TF rod current as has typically been observed.

3.4. Comparison of halo current widths to analytic estimates

Reference [40] derives an approximate formula for the halo width, based on Bohm diffusion or electrostatic turbulence: $\Delta_h \sim 3.5\,\mathrm{cm}\sqrt{q_h R_0 T_h^{1/2}/B_0}$. Typical parameters for NSTX are $R_0 = 1.0$ m, $B_0 = 0.5$ T, $q_h \sim 2.5$. The value of q_h comes from calculations of the edge safety factor at the onset of a VDE disruption. The halo temperature T_h is not measured in NSTX, and thus a range should be considered. For $T_h = 10$ eV, this expression yields $\Delta_h = 14$ cm, while $T_h = 40$ eV, this expression yields $\Delta_h = 20$ cm. These are within a factor of 2 of the approximate values at midplane for the NSTX cases, which is as reasonable agreement as can be expected given the approximations in both the experiment and model.

4. Database analysis

In this section, we present database analysis of a large number of discharges during the 2008–2010 campaigns. Note that all data in these plots have toroidal field in the common direction (downward rod current). The results of a toroidal field reversal on the halo currents are described in section 5.

4.1. Relationship between the halo current magnitude and toroidal peaking in NSTX

In general, it has been found that the halo current fraction and toroidal peaking factor are anti-correlated. For instance, figure 64 of [2] shows that the data from many conventional aspect ratio tokamaks can be bound by the relationship:

$$\frac{I_{h,\max}}{I_P}\mathrm{TPF} < 0.75. \quad (1)$$

A somewhat similar result was shown for the MAST ST (see figure 7 of [62]).

We have conducted a similar analysis for the NSTX data, in this case sorting the data by the various different measurement locations. The results of this analysis are shown in figure 7, where again, only cases with the standard toroidal field direction (TF rod current flowing downwards) are shown. In each case, the data are sampled at the time of maximum halo current. Also shown in solid or dashed lines are curves of the form $\mathrm{TPF} = 1 + C/\mathrm{HCF}$ and $1 + C/(2 \cdot \mathrm{HCF})$, where C is a constant adjusted for each sensor array (and HCF is the halo current fraction, defined as I_{halo}/I_P). The values of the constant C are indicated in the bottom left of each frame. Note that this form is somewhat different than in equation (1), but is advantageous in not allowing peaking factors less than 1 and in forming a tight bound on the NSTX data. We also show

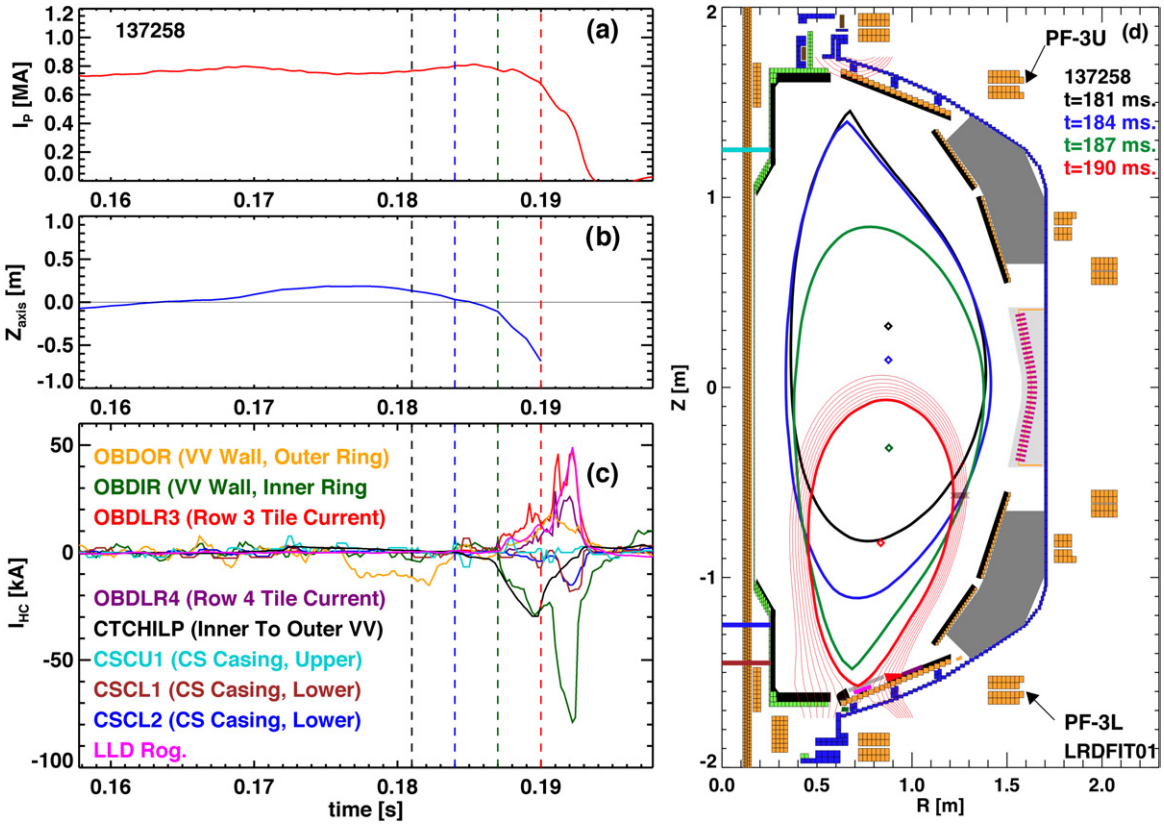

Figure 5. Evolution of the halo currents and plasma boundary for a disruption that limits on the lower outboard divertor. The individual frames contain the same data as figures 2 and 3.

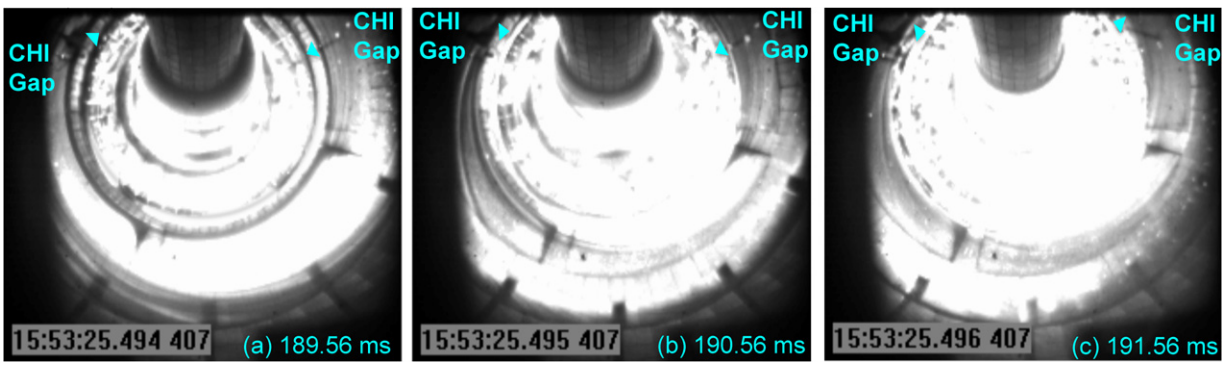

Figure 6. Images of the lower divertor region during the downward VDE disruption illustrated in figure 5. The CHI gap, illustrated by the circle in (*a*), fills with plasma (*b*) and (*c*). As described in the text, this plasma conducts a significant fraction of the poloidal halo current.

in frames (*b*)–(*e*) the dotted line determined by converting equation (1) to an equality.

It is clear from this analysis that NSTX follows a trend similar to that in other spherical and conventional aspect ratio tokamaks, with the large halo currents being more toroidally uniform than those cases with smaller currents. However, it is interesting to move beyond this simple observation, and look at the data for each sensor array individually.

Frame (*a*) shows the data for the CSC Rogowski CSCL1. The points on the left side of the HCF = 0 correspond to downward-going disruptions, such as is illustrated in figure 5. It is very rare for the vertically displaced plasma to limit on the centre column; the vastly more common result is for the plasma to limit on the outboard divertor. Hence, only the far region of the halo supplies current to the centre column in these cases. The halo current fractions are correspondingly small. The points on the right of HCF = 0 are due to upward disruptions, which can provide current in the lower centre column via the mechanism discussed in regard to figure 2. These cases collected current from the entire horizontal part of the upper divertor, such that halo current fractions of 7–8% are not uncommon, compared to 3–4% for the downward-going VDEs.

Frames (*b*) and (*c*) show the same data, for the inner and outer rings of toroidal field detectors. The data with HCF > 0 in these two frames correspond to the same upward disruptions as in the previous paragraph, and show the same limit of 7–8% of the flat-top plasma current. The data on with HCF < 0

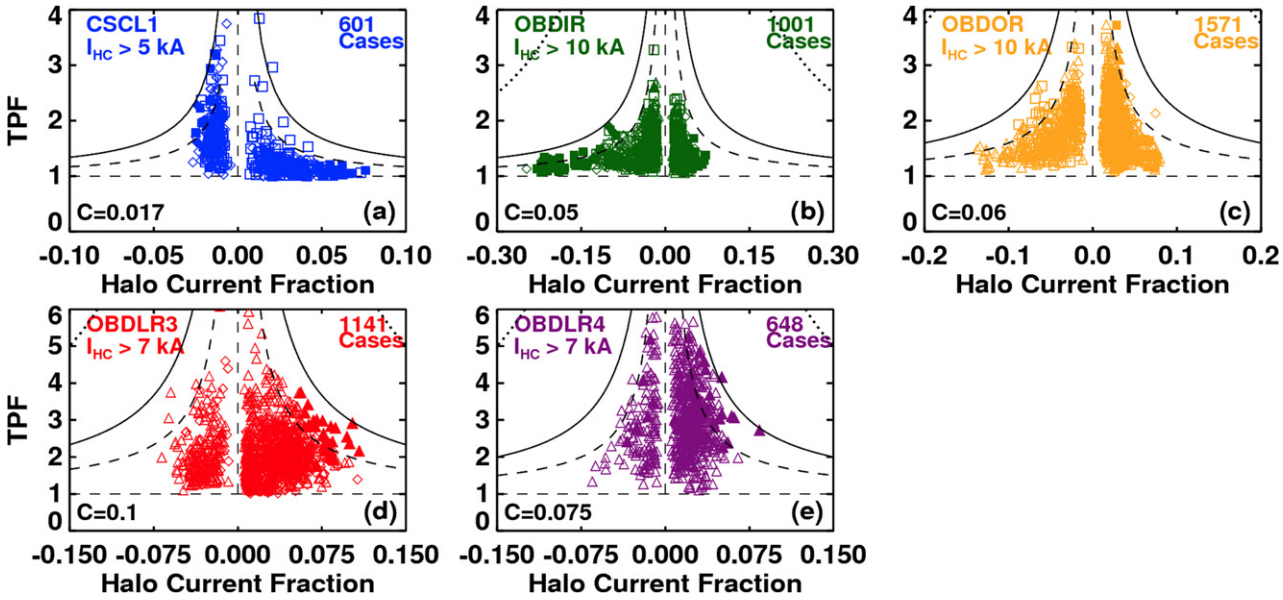

Figure 7. Halo current fractions versus toroidal peaking factors (TPFs), for a large number of NSTX disruptions. Solid points correspond to deliberate VDEs, while open points are inadvertent disruptions. See text for explanation of the contours and data selection criterion.

for the outer ring in frame (*b*) correspond to downward VDEs similar to that shown in figure 5. Halo currents in the chamber wall of up to 25% of the flat-top plasma current have been observed in this location (the lower vessel wall), with both deliberate and inadvertent VDEs providing data at this limit. The outer ring points with HCF < 0 in frame (*c*) are for disruptions like in figure 3, where the plasma limits on the lower secondary passive plate, and some current flows into the lower outboard divertor, through the vessel, and returns to the plasma through the plate. The currents in the vessel wall for this class of disruption have been observed with magnitudes up to 15% of the flat-top I_P, and it is certainly true that there are some unmeasured currents local to the secondary passive plate in these cases.

Finally, frames (*d*) and (*e*), show the peaking factors and halo current fractions for the arrays of shunt tiles in rows 3 and 4 of the outboard divertor. HCF > 0 in this case corresponds to cases such as figure 5, where the plasma limits on the lower outboard divertor. In these cases we see up to 10% of the plasma current flowing directly into a row of tiles ∼11 cm in radial dimension, at a major radius of 0.9 and 1.0 m for the rows three and four. The HCF < 0 cases are for plasmas that limit on the secondary passive plates as in figure 3, and up to ∼5% of the plasma current is observed to flow into those tiles for these cases.

Finally, it appears that the NSTX values fall below the worst case suggested from equation (1), at least for those components that have been instrumented. We caution that the diagnostic set is not sufficiently complete to assess the total halo current flowing simultaneously into all components, and it is thus inappropriate to compare these results to data which tabulate the TOTAL halo current flowing in all components. Indeed, the total halo current on any given disruption is significantly larger than that inferred from any individual point below. Note, however, that the force on any particular component is determined by the local halo current, and so breaking the data into the individual locations may be more useful than showing the total.

Given that the data in figure 7 are sampled at the time of maximum halo current, it appears possible that the product of the halo current fraction and toroidal peaking factor could be larger at some other time during the evolution of the disrupting plasma. We evaluate this by plotting the time trajectory of the HCF and TPF for a series of discharges in figure 8. Each column corresponds to a given sensor array, and six discharges are indicated in each column. The discharges are not the same for each column, and are chosen to indicate cases that approach the maximum values of HCF × TPF for each detector array. Also indicated in the figure is whether a given discharge was a deliberate VDE (all cases have the conventional TF polarity). There is a star at the point of maximum HCF. We see that the point at maximum HCF tends to coincide with the point of largest HCF × TPF. The data in this figure thus indicate that the data selection method in figure 7 is reasonable.

The detailed trajectories show that for the arrays measuring the currents in the chamber wall, the peaking factors tend to be low once the currents grow. The evolution is mostly to and from larger values of HCF at low values of TPF. The arrays measuring the current entrance points, however, show a much more complicated evolution, rapidly evolving between states with larger TPF and or larger HCF. The implication of these observations is that the current dynamics at the entrance and exit points in the divertor tiles may be fairly complicated, but that current becomes more uniform once it enters the chamber walls. This effect was previously seen in simulations [25].

Table 2 provides some characteristic data regarding the discharges in figure 8. The q_{95}, κ and β_N values are taken as either the typical value during the I_P flat-top, or, if the disruption occurs during the current ramp, the value of these parameters achieved just before the discharge failed. The data in this table and the previous figure allow an assessment of the conditions that promote large halo currents. For the OBDIR,

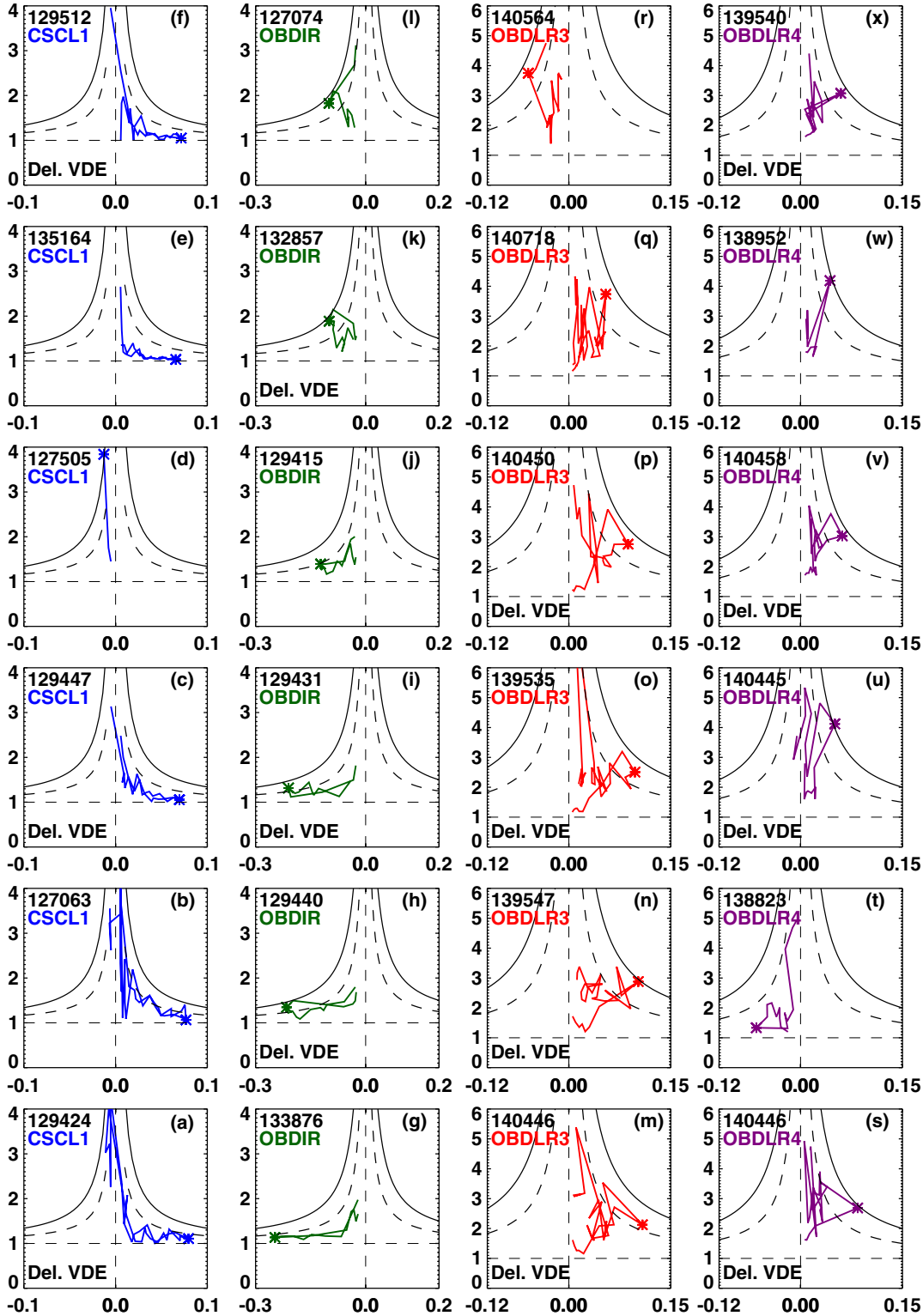

Figure 8. Time evolution of the TPF versus HCF, for six discharges in each of four detector arrays. The black contour lines are the same as in figure 7.

OBDLR3 and OBDLR4 arrays, a large fraction of the worst cases are deliberate (and sometime strongly driven) L-mode VDEs, which tend to have very rapid vertical motion. These detectors are ideally placed to detect the currents for these cases, whose shape evolution tends to be broadly similar to that depicted in figure 5.

There are, however, a significant number of non-deliberate VDEs that match these cases for large halo current fractions. Interestingly, these were typically not the scenarios with the highest-β and κ. Rather, they were often disruptions during the I_P ramp or at the start of plasma current flat-top (SoFT), before the stored energy is largest. This trend will be observed again

Table 2. Characteristics of selected discharges that produced very large halo currents. These discharges are the same as in figure 8. Here, 'LoC' refers to loss of $n = 0$ (vertical position) control, while SoFT mean start of the I_P flat-top. Here, δ stands for triangularity, and the units of β_N are (%mT MA^{-1}).

Shot	I_P (kA)	q_{95}	κ	β_N	Heating	Vertical control response	Time in discharge	Frame in figure 8
129512	620	5.3	1.9	0.5	Ohmic	Freeze and push down	I_P FT	(*f*)
135164	800	8	2	5	$P_{NBI} = 5$ MW	LoC	I_P FT	(*e*)
127505	900	9.8	2.2	2.5	$P_{NBI} = 4$ MW	LoC	I_P FT	(*d*)
129447	620	4.7	1.9	1.0	Ohmic	Freeze and push down	I_P FT	(*c*)
127063	450	10	1.9	0.4	Ohmic	LoC	I_P Ramp-Up	(*b*)
129424	500	10	1.7	0.5	Ohmic	Freeze and push down	I_P FT	(*a*)
127074	580	8	1.9	1.0	Ohmic	Freeze	I_P FT	(*l*)
132857	600	8	1.9	0.8	Ohmic	Freeze and push down	I_P FT	(*k*)
129415	600	9	1.9	0.8	Ohmic	Freeze	I_P FT	(*j*)
129431	590	6.3	1.8	0.5	Ohmic	Freeze	I_P FT	(*i*)
129440	580	6	1.8	0.9	Ohmic	Freeze	I_P FT	(*h*)
133876	750	6.5	2.1	3.2	$P_{NBI} = 6$ MW	LoC	SoFT	(*g*)
140564	660	8	2.3	1.5	$P_{NBI} = 4$ MW	LoC	SoFT	(*r*)
140718	700	14	2.6	5.1	$P_{NBI} = 5$ MW	LoC	I_P FT	(*q*)
140450	580	8	1.9	1.0	Ohmic	Freeze and push down	I_P FT	(*p*)
139535	600	10	2.0	2.5	$P_{NBI} = 1$ MW	Freeze and push down	I_P FT	(*o*)
139547	500	10	1.6	1.8	$P_{NBI} = 2$ MW	Freeze and push down	I_P FT	(*n*)
140446	600	9.2	1.9	1.0	Ohmic	Freeze and push down	I_P FT	(*m*), (*s*)
139540	580	9	1.9	0.9	Ohmic	Freeze and push down	I_P FT	(*x*)
138952	750	9	1.9	6.2	$P_{NBI} = 4$ MW	LoC	I_P FT	(*w*)
140458	650	7.2	1.9	2.2	$P_{NBI} = 2$ MW	Freeze and push down	I_P FT	(*v*)
140445	650	7.5	1.8	1.1	Ohmic	Freeze and push down	I_P FT	(*u*)
138823	900	8.5	2.3	4.0	$P_{NBI} = 3$ MW	LoC	I_P FT	(*t*)

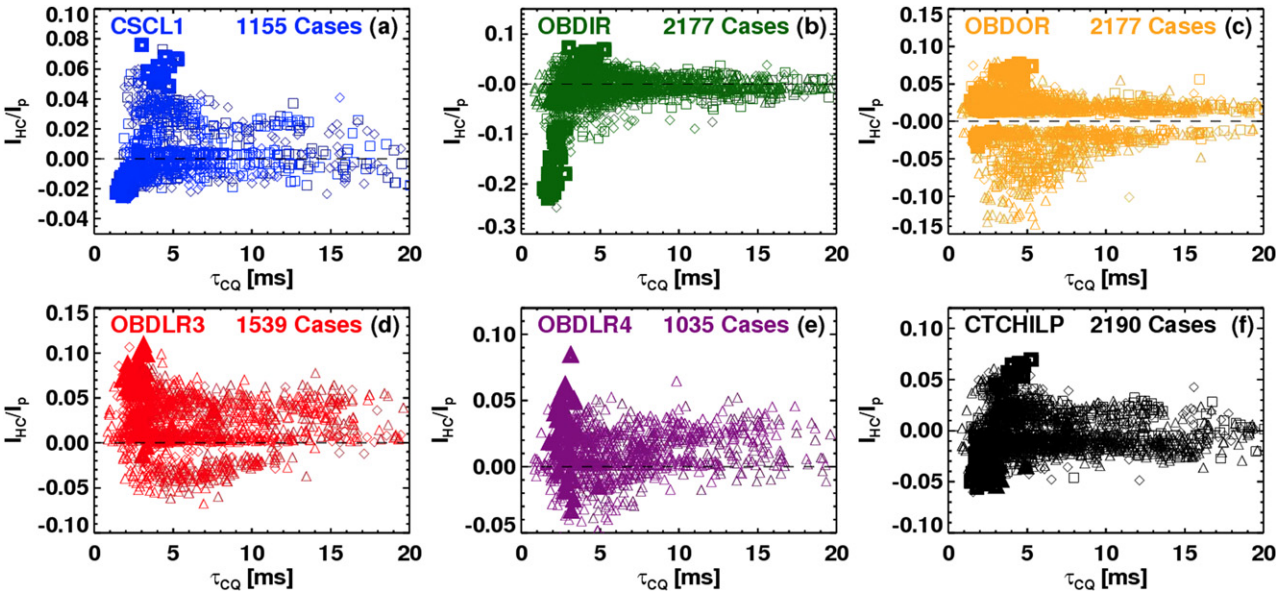

Figure 9. Halo current fraction plotted against the current quench time. The largest halo currents often occur in discharges with the fastest current quenches.

in the context of figure 14, where it is shown that discharges with less stored energy just before the disruption often have larger halo currents than cases with large values of stored energy.

4.2. Scaling of the halo current fraction with the plasma current quench rate

Results from JET indicate that the halo currents are typically smaller in discharges with rapid I_P quenches (see figure 3 of [33]). This assumption has additionally been applied to ITER simulations (see discussion on page 339 of [13]). The NSTX data, however, show a different trend.

Figure 9 shows the halo current fraction at the various diagnostics, as a function of the current quench time. Here, the current quench time is defined by $\tau_{CQ} = \frac{5}{3}(t_{20} - t_{80})$, where t_{80} and t_{20} are the times when the plasma current has decayed to 80% and 20% of the pre-disruption value [6]. This choice of variables is made based on the notion that the halo currents are driven by a flux change: $I_{HC} \propto d\psi/dt$. The choice of plotted variables then follows by noting that the flux available to drive the current is proportional to the plasma current, and that the

current quench time is an important representative time scale in the problem.

Considering first the current on the lower centre column in frame (*a*), the largest positive (for upward VDEs) and negative (for downward VDEs) halo current fractions occur for the fastest quenches. The vessel wall currents measured by the 'inner ring' detectors (OBDIR detectors) are shown in frame (*b*), and show the largest halo currents for disruptions with I_P quench times of 1–3 ms. Many of these cases are triggered VDEs (solid symbols) similar to that in figure 5, that were produced in 2008 before the shunt tile arrays were installed. The envelope of inadvertent VDEs and disruptions, however, shows the same trend. The outer-ring detectors (OBDOR) were not excited by these triggered VDEs, but show a similar trend for the inadvertent VDEs. Positive signals correspond to upward VDEs as in figure 2, while negative signals are for downward VDEs which impact the secondary passive plates, as in figure 3. In both cases, the observed halo currents are strongest for fast quenches.

One might reasonably be concerned that the large eddy currents induced during the current quench might contaminate the B_T measurements that underlie the CSCL1, OBDIR and OBDOR signals. The shunt tile arrays OBDLR3 and OBDLR4, however, are insensitive to magnetic field pickup. These two arrays show a similar result, with fast quenches often yielding the largest halo currents. Finally, the current linking the inner and outer vessels, designated CTCHILP, is measured with a transducer located underneath the vessel. It also shows the largest halo current fractions for cases with rapid current quenches.

As noted above, this trend is counter to what is observed in many other devices, The general expectation from those devices is that disruptions with very rapid current quenches will not move significantly before the plasma current, and hence drive for the halo currents, has decreased significantly. This assumption is often incorrect for NSTX. Most disruptions in NSTX to date have significant vertical motion of the plasma column before the final thermal and current quenches, and many of the fastest current quenches occur after the plasma has already made contact with the divertor plate. This underscores the role that the dynamics of the vertical position control system play in determining the halo current level.

Finally, we note that for all detectors, there are cases where fast current quenches occur, but the observed halo current fraction is low. There are two reasons for this. Firstly, there is a small subset of fast current quenches that occur with the plasma centred in the vessel, and thus produce very small halo currents. Secondly, whether a given detector observes currents depends on the details of the plasma motion, as described in relation to figures 3 and 5. Many points with small halo currents in figure 9 are simply a consequence of that particular detector not being located to measure the currents for a particular discharge.

4.3. Time duration of the halo current pulse

The halo current pulse has a finite duration, during which it exerts a force on the vacuum chamber and/or vessel components. In order to quantify this time duration, we have used an area equivalent definition to compute the duration of the halo current pulse:

$$\tau_{\mathrm{HCF}\times\mathrm{TPF}} = \frac{\int (\mathrm{HCF} \times \mathrm{TPF})\, \mathrm{d}t}{\max(\mathrm{HCF} \times \mathrm{TPF})}. \quad (2)$$

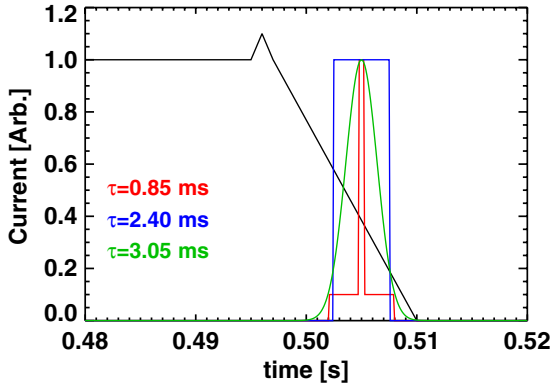

Figure 10. Example of the area equivalent definitions for the duration of the halo current pulse. The three pulses have the same amplitudes, but different effective durations.

With this definition, the local impulse can be estimated as $L \cdot \mathrm{TPF} \cdot I_H B_T \tau_{\mathrm{HCF}\times\mathrm{TPF}}$, where L is the length of the halo current path in the component of interest. Examples of the calculation in equation (2) are shown in figure 10, for three different model halo current pulses of similar peak amplitude, but different waveform shapes.

Using this definition, we have compared the effective duration of the halo current pulse to the current quench time τ_{CQ}. We have chosen τ_{CQ} because it parametrizes the time-scale of the current quench, which is thought to be a prominent driver of disruption halo currents [26]. The result of this analysis is shown in figure 11, where the data have again been separated as per the different halo current detection arrays.

For most cases, the current quench time is significantly longer than the halo current pulse. This is because the current decay often begins before there is any substantial contact with the lower divertor; that there are often multiple timescales associated with the current quench has been documented for NSTX [7], as well as other devices [5]. On the other hand, for the fastest quenches, the effective duration of the halo current can be larger than the current quench. These are typically cases where there is very little plasma current reduction during the vertical motion proceeding the thermal quench, as in a 'pure' VDE. There is a substantial halo current before the plasma current begins to decay in these cases, and some halo current is maintained throughout the current quench. In general, the effective duration of the halo currents, at least with regard to the impulse they apply, is in the vicinity of 1–5 ms.

The data in figure 11, along with the definition in equation (2), allow the total impulse to be studied as a function of various parameters. A metric proportional to this impulse is shown in figure 12, plotted against the plasma current just before the disruption; in particular, the quantity $\mathrm{TPF} \cdot I_H \cdot \tau_{\mathrm{HCF}\times\mathrm{TPF}}$ can be converted to impulse when multiplied by the toroidal field and path length. Consider first the magnetic field based detection in the upper row. Upward VDEs that drive halo currents around the total poloidal circumference of the vessel

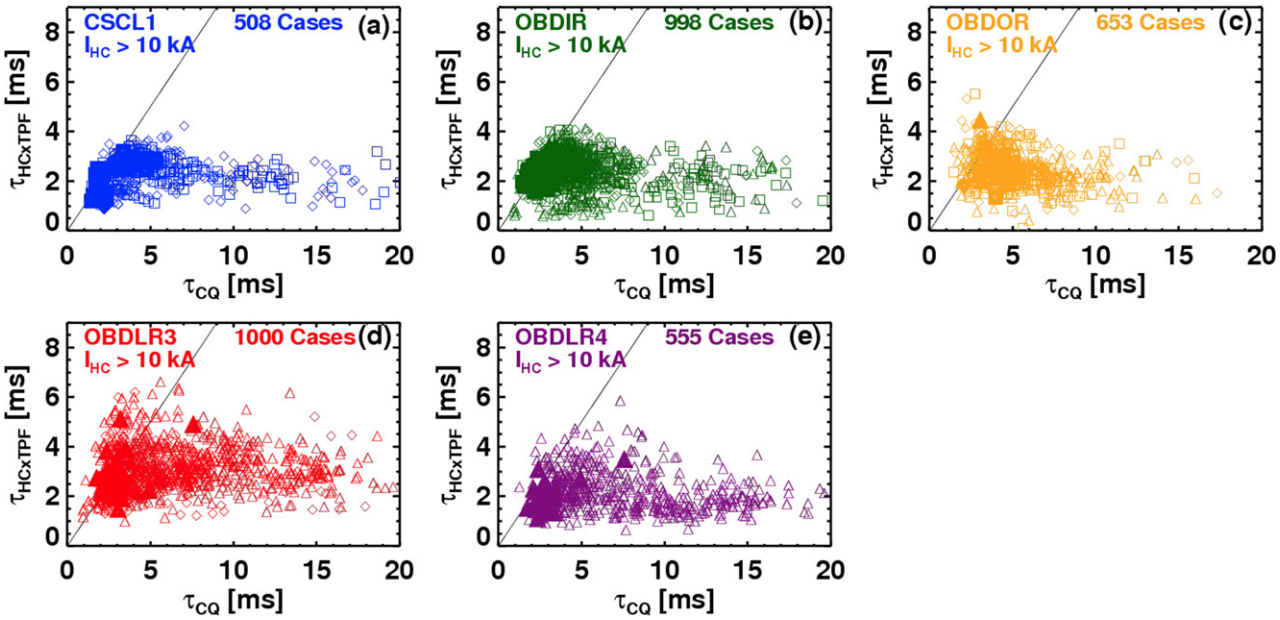

Figure 11. Halo current pulse duration compared to current quench duration.

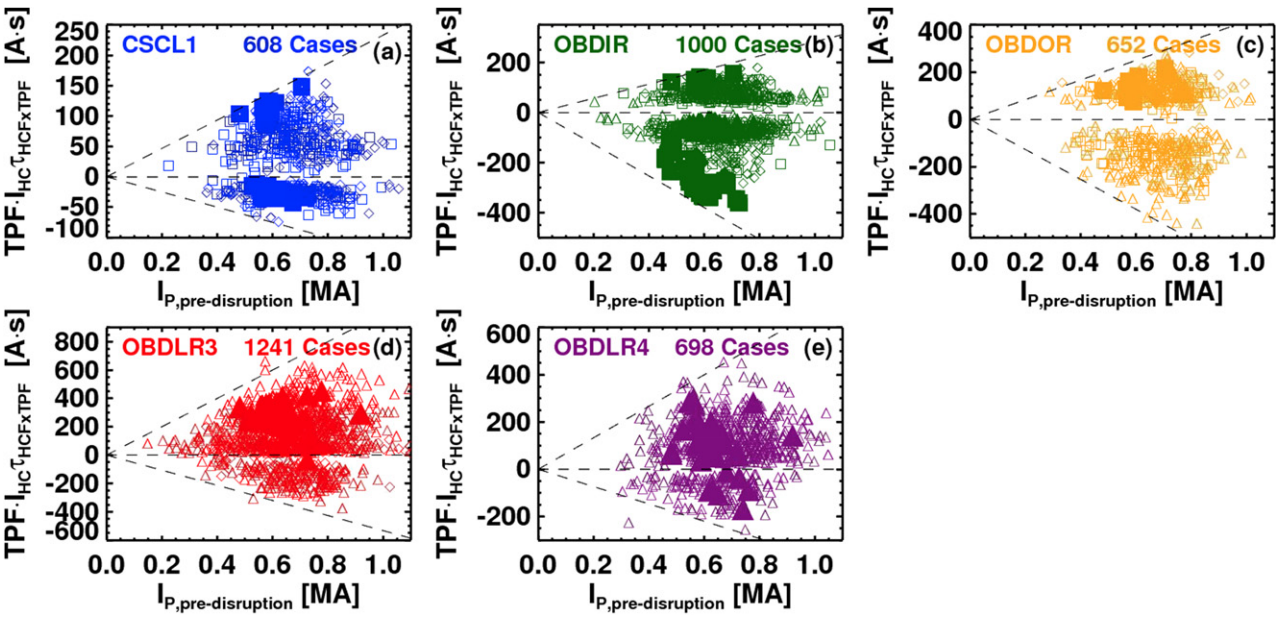

Figure 12. The quantity TPF · I_H · $\tau_{HCF\times TPF}$, proportional to the local halo current impulse, plotted against the pre-disruption plasma current.

correspond to positive values in frames (*a*)–(*c*). Downward VDEs correspond to negative values of impulse in these cases. As indicated by the dashed lines, both directions show a magnitude of impulse whose envelope is proportional to the plasma current.

Frames (*d*) and (*e*) show data from the shunt tile arrays. These data show the same bounding trend, most clearly in the positive impulse side of the frames. These points correspond to measurements near the VDE limiting point for downward VDEs impacting the divertor floor, as in figure 5.

The vast majority of the points in figure 12 have $I_P < 1000$ kA. For the L-mode and low power H-mode deliberate VDEs, the maximum achievable current is ~800 kA. High-power H-modes in the database have commonly been run with up to 1300 kA of current in this data set. These cases tend to have a rather large current loss before the actual final disruption. When we have plotted the data against the value of the plasma current at the time of maximum stored energy, we have found the bounding relationship described in the previous paragraphs to be less crisp.

This impulse-like quantity can then be compared to the current quench time. Figure 13 shows this relationship, where TPF · I_H · $\tau_{HCF\times TPF}$ has the normalized to the flat-top plasma current. We see once again that the largest impulses often occur for the fast current quenches. Hence, it is important to consider the simultaneous maximum halo current and eddy currents loads when designing the in-vessel structures for next-step STs.

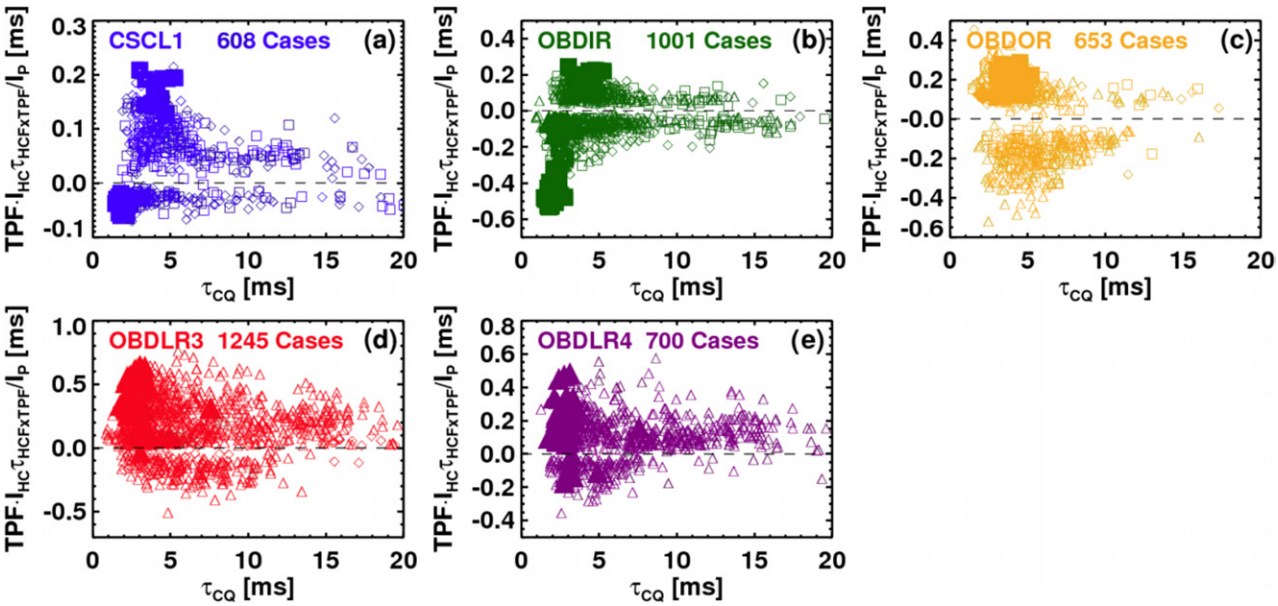

Figure 13. The quantity TPF · I_H · $\tau_{HCF\times TPF}/I_P$ compared to current quench duration, for six different locations around NSTX. This quantity is proportional to the impulse normalized by the plasma current.

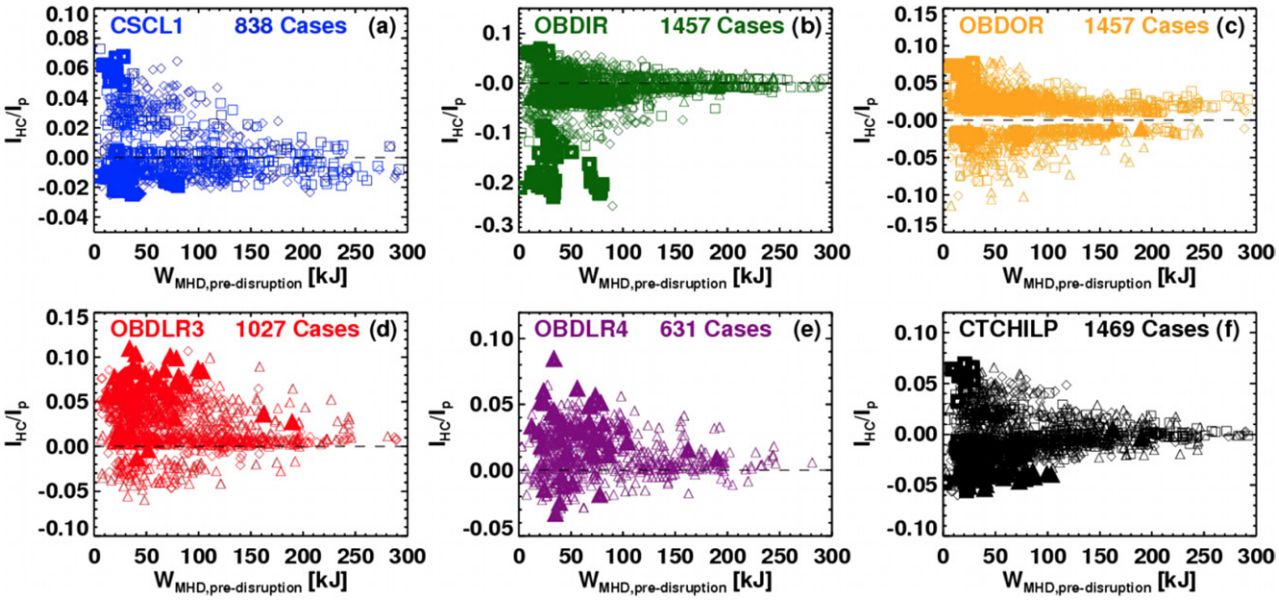

Figure 14. Halo current fraction plotted against the pre-disruption stored energy.

4.4. Relationship between halo current magnitudes and the pre-disruption stored energy

It has been noted in previous work from JT-60 [27] that large halo currents tend to anti-correlate with large pre-disruption stored thermal energy. We find a similar trend in NSTX, as evidenced by the analysis in figure 14.

In this case, the pre-disruption stored energy is computed using the EFIT reconstructions that are computed for each discharge. The time of the disruption current quench is automatically found [7], and then the last good stored energy is recorded if it is within 15 ms of the disruption. Not all cases have a good reconstruction within this time window, and those discharges are not included in the plots.

For all detector systems, we find that the largest halo currents occur for plasmas with smaller pre-disruption stored energies. Large halo currents are almost never observed for cases with pre-disruption $W_{MHD} > 200$ kJ (the maximum stored energy ever achieved in NSTX is ~470 kJ [44]). We have also plotted the data against the maximum stored energy at any time during the discharge. While the trend shown in figure 14 (reduced halo current at large energy) remains visible, it is much less clear. Hence, it is clear, and intuitive, that the stored energy just prior to the disruption is the relevant quantity. It has been speculated that plasmas with large pre-disruption stored energy create more impurities during the phase of the disruption proceeding the halo currents, thus increasing the halo resistance [27]; the present data are consistent with that

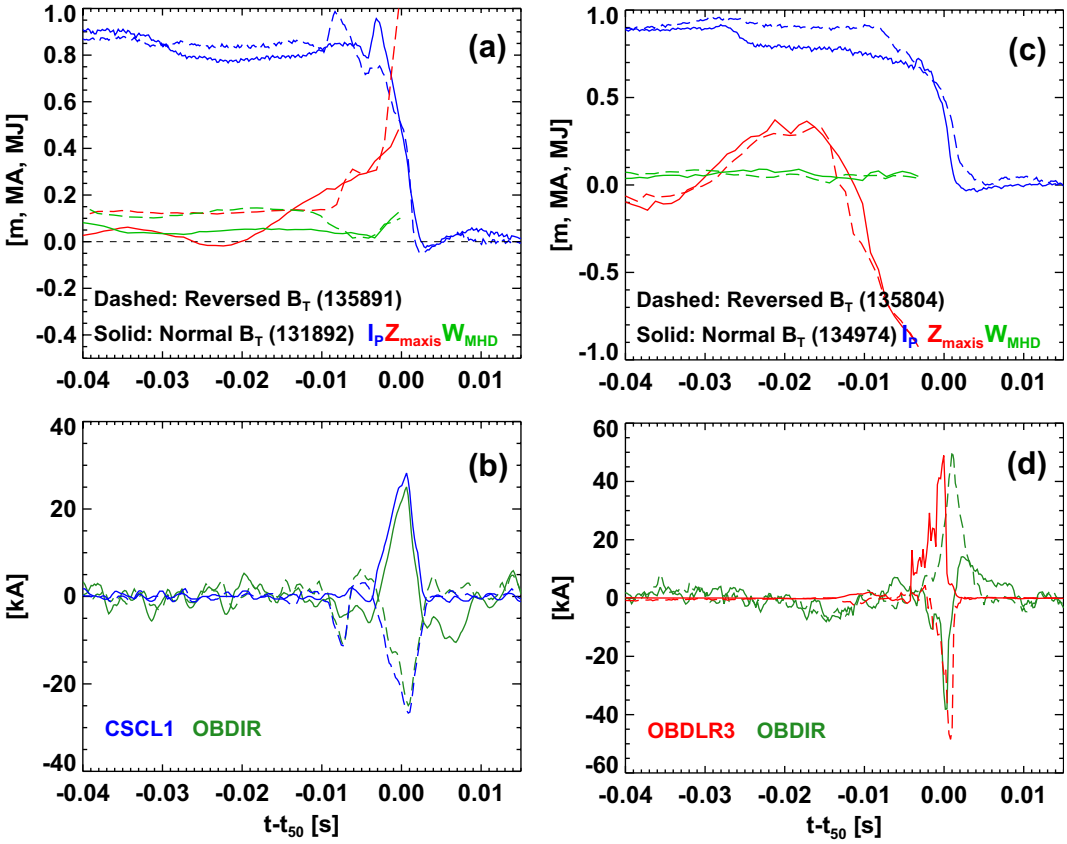

Figure 15. Reversal of halo currents with B_T reversal, for upward (left column) and downward (right column) disruptions. (*a*) and (*c*) show the plasma current (MA), stored energy (MJ), and the vertical position of the magnetic axis (m). (*b*) and (*d*) show the signal in various halo current detector systems. Solid lines are for the standard toroidal field polarity (clockwise when viewed from above), while dashed lines are for reversed toroidal field.

hypothesis, though without reliable and routine measurements of the halo temperature and resistivity, this suggestion remains an untested hypothesis. Additionally, plasmas that disrupt at large stored energy and high β_N in NSTX are often more centred in the vessel through the disruption process, compared to those which have large pre-disruption stored energy loss or that disrupt earlier in the discharge.

5. Effect of toroidal field reversal on poloidal halo currents

Early work on disruption halo currents suggested that the $n = 0$ part of the halo current acts to stabilize the plasma vertical motion [24]. An implication of this suggestion is that if the toroidal field direction is reversed, the poloidal component of the halo current should reverse as well, though this hypothesis was not tested in [24].

NSTX completed a 3 week run period during the 2008 campaign with the toroidal field reversed. Figure 15 shows a comparison of the time evolution of $n = 0$ toroidally average halo currents for forward and reversed toroidal field cases, in otherwise similar upward (left column) and downward (right column) disruptions. In each column, the upper figure shows the plasma current, magnetic axis location, and stored energy, while the bottom row shows the halo currents. The solid curves correspond to the case with standard toroidal field (clockwise from above), while the dashed curves correspond to reversed toroidal field. In all cases, time is referenced to the instant when the plasma current has decreased to 50% of the pre-disruption value.

Considering the upward VDE in the left column first, the halo current magnitude is similar for the two signs of toroidal field, but the sign is reversed. For instance, in frame (*b*), the blue solid line, corresponding to the centre-column Rogowski and standard B_T direction, has the same magnitude but opposite sign of the dashed blue line, corresponding to the same sensors but reversed B_T. Similarly the green traces, corresponding to the inner ring of B_T detectors, have similar magnitudes but opposite signs when the toroidal field is reversed.

The same trend is visible in the right column, corresponding to the downward VDE. The currents detected by the ring of toroidal field detectors or the row-3 shunt tiles are similar in the two cases, but the signs are reversed.

6. Summary and discussion

This paper has described measurements of the disruption halo current in NSTX. Important results and findings include

- documentation of different halo current paths pending the dynamics of the vertical motion,
- illustration of plasmas between components forming part of the halo current path,

- determination of the statistical relationship between the peaking factor and halo current fractions for different locations in the device, and specific examples of different trajectories in this space,
- confirmation of low halo current fractions and peaking factors on the centre column, where the toroidal field is highest,
- observation of larger halo current magnitudes and impulses in cases with faster current quenches,
- reduced halo currents in cases with large pre-disruption stored energy, and
- reversal of the poloidal current direction when the toroidal field is reversed.

These results are generally positive for the ST, in that the worst-case estimates of the halo current loading based on conventional aspect tokamaks results (equation (1)) may be overly conservative for an ST. Especially important is the observation that the peaking factors on the lower centre column are fairly low. These results are similar to those from MAST [62]. We note, however, that there are no measurements of midplane centre-column halo currents in NSTX. Some current likely flows on the centre column when a vertically centred plasma is pushed inwards and disrupts, and these currents have not been resolved in NSTX.

However, further studies are clearly required in order to fully understand and predict the halo current dynamics forces. Detailed measurements of the halo temperature [89] are quite rare, and are unavailable in NSTX. Knowledge of this parameter, along with the effective width of the halo, would provide a better understanding of the trends in, for instance, figure 14.

A key limitation in these studies is the lack of an equilibrium code that can accurately model the plasma state in the presence of a significant halo current. Typical Grad–Shafranov based reconstruction codes only allow plasma currents inside the magnetic separatrix; using codes with this constraint in the presence of large currents outside the separatrix is bound to introduce some errors. Historically, this problem has been solved using filament-model reconstructions [26], which do not involve a force balance constraint. However, the slow time-scale of the disruption compared to the Alfven time implies that an MHD equilibrium, possibly with significant 3D features, must exist [40]. It would be quite useful to have an equilibrium reconstruction code that could take into account the measured halo currents when reconstructing an approximate 2D, or fully 3D, equilibrium solution.

The dynamics of the halo current non-axisymmetries are also potentially more complicated than can be inferred from plots of the peaking factor and halo current fraction. Significant toroidal rotation of the halo current asymmetry has been observed in ALCATOR C-MOD [28] and JET [90, 91], though not in AUG [37]. This rotation has the potential to resonate with mechanical structures, increasing the potential for structural damage. We have observed significant toroidal rotations of the halo current non-axisymmetry in NSTX, with 5–7 toroidal circuits in rare case. These dynamics will be described in a future publication.

Acknowledgments

The authors would like to thank Henry Kugel, Robert Kaita, Eric Fredrickson, and Hiro Takahashi for assistance and advice regarding the design and fabrication of the halo current detection diagnostics. This research was funded by the United States Department of Energy.

References

[1] Wesson J. 1997 *Tokamaks* (Oxford: Clarendon)
[2] ITER Physics Basis 1999 *Nucl. Fusion* **39** 2137
[3] Hender T.C. *et al* and the ITPA MHD 2007 Progress in the ITER Physics Basis Chapter 3: MHD stability, operational limits and disruptions *Nucl. Fusion* **47** S128–202
[4] Humphreys D.A. and Whyte D.G. 2000 *Phys. Plasmas* **7** 4057
[5] Riccardo V., Barabaschi P. and Mugihara M. 2005 *Plasma Phys. Control. Fusion* **47** 117
[6] Wesley J.C. *et al* 2006 *Proc. 21st Int. Conf. on Fusion Energy 2006 (Chengdu, China, 2006)* (Vienna: IAEA) CD-ROM file IT/P1-21 and http://www-naweb.iaea.org/napc/physics/FEC/FEC2006/html/index.htm
[7] Gerhardt S.P., Menard J.E. and the NSTX Team 2009 *Nucl. Fusion* **49** 025005
[8] Wesley J.C. *et al* 2010 *Proc. 23rd Int. Conf. on Fusion Energy 2010 (Daejeon, South Korea 2010)* (Vienna: IAEA) CD-ROM file ITR/P1-26 and http://www-naweb.iaea.org/napc/physics/FEC/FEC2010/html/index.htm
[9] Shibata Y. *et al* and the JT-60 team 2010 *Nucl. Fusion* **50** 025012
[10] Riccardo V., Andrew P., Ingesson L.C. and Maddaluno G. 2002 *Plasma Phys. Control Fusion* **44** 905
[11] Arnoux G., Loarte A., Riccardo V., Fundamenski W., Huber A. and JET-EFDA contributors 2009 *Nucl. Fusion* **49** 085038
[12] Riccardo V. *et al* and JET-EFDA contributors 2010 *Plasma Phys. Control. Fusion* **52** 124018
[13] Sugihara M., Shimada M., Fujieda H., Gribov Yu., Ioki K., Kawano Y., Khayrutdinov R., Lukash V. and Ohmori J. 2007 *Nucl. Fusion* **47** 337
[14] Rosenbluth M.N. and Putvinski S.V. 1997 *Nucl. Fusion* **37** 1355
[15] Yoshino R., Tokuda S. and Kawano Y. 1999 *Nucl. Fusion* **39** 151
[16] Yoshino R. and Tokuda S. 2000 *Nucl. Fusion* **40** 1293
[17] Gill R.D., Alper B., de Baar M., Hender T.C., Johnson M.F., Riccardo V. and contributors to the EFDA-JET Workprogramm 2002 *Nucl. Fusion* **42** 1039
[18] Tamai H., Yoshino R., Tokuda S., Kurita G., Neyatani Y., Bakhtiari M., Khayrutdinov R.R., Lukash V.E., Rosenbluth M.N. and JT-60 Team 2002 *Nucl. Fusion* **42** 290
[19] Plyusnin V.V., Riccardo V., Jaspers R., Alper B., Kiptily V.G., Mlynar J., Popovichev S., de La Luna E., Andersson F. and JET EFDA contributors 2006 *Nucl. Fusion* **46** 277
[20] Forster M., Finken K.H., Lehnen M., Linke J., Schweer B., Thomser C., Willi O., Xu Y. and the TEXTOR team 2011 *Nucl. Fusion* **51** 043003
[21] Sizyuk V. and Hassanein A. 2009 *Nucl. Fusion* **49** 095003
[22] Schaffer M.J. and Leikund B.J. 1991 *Nucl. Fusion* **31** 1750
[23] Strait E.J., L.L Lao, Luxon J.L. and Reis E.E. 1991 *Nucl. Fusion* **31** 527
[24] Andrew P. Noll P. and Riccardo P.V. 1997 *Proc. 17th IEEE/NPSS Symp. on Fusion Engineering (San Diego, CA, 6–10 October 1997)* p 108 http://ieeexplore.ieee.org/stamp/stamp.jsp?tp=&arnumber=685673
[25] Pomphrey N., Bialek J.M. and Park W. 1998 *Nucl. Fusion* **38** 449
[26] Humphreys D.A. and Kellman A.G. 1999 *Phys. Plasmas* **6** 2742
[27] Neyatani Y., Yoshino R., Nakamura Y. and Sakurai S. 1999 *Nucl. Fusion* **39** 559

[28] Granetz R.S., Hutchinson I.H., Sorci J., Irby J.H., LaBombard B. and Gwinn D. 1996 *Nucl. Fusion* **36** 545
[29] Knight P.J., Castle G.G., Morris A.W., Caloutsis A. and Gimblett C.G. 2000 *Nucl. Fusion* **40** 325
[30] Pautasso G. and Gruber O. 2003 *Fusion Sci. Technol.* **44** 716
[31] Riccardo V., Lam N., Lawler A., Starkey D. and Contributors to the EFDA-JET Workprogramme 2003 *Fusion Eng. Des.* **66–68** 919
[32] Riccardo V. and JET EFDA contributors 2003 *Plasma Phys. Control. Fusion* **45** A269
[33] Riccardo V., Hender T.C., Lomas P.J., Alper B., Bolzonella T., de Vries P., Maddison G.P. and the JET EFDA Contributors 2004 *Plasma Phys. Control. Fusion* **46** 925
[34] Zakharov L.E. 2008 *Phys. Plasmas* **15** 062507
[35] Riccardo V. *et al* and JET EFDA Contributors 2009 *Nucl. Fusion* **49** 055012
[36] Eidietis N.W. and Humphreys D.A. 2010 *Proc. 23rd Int. Conf. on Fusion Energy 2010 (Daejeon, South Korea 2010)* (Vienna: IAEA) CD-ROM file EXS/P2-05 and http://www-naweb.iaea.org/napc/physics/FEC/FEC2010/html/index.htm
[37] Pautasso G., Giannone L., Gruber O., Herrmann A., Maraschek M., Schuhbeck K.H. and the ASDEX Upgrade Team 2011 *Nucl. Fusion* **51** 1
[38] Pautasso G. *et al* and the ASDEX Upgrade Team 2011 *Nucl. Fusion* **51** 094012
[39] Zakharov L.E. 2011 *Phys. Plasmas* **18** 062503
[40] Boozer A.H. 2012 Physics of tokamak disruption simulations *Phys. Plasmas* at press
[41] Lazarus E.A. *et al* 1991 *Phys. Fluids* **3** 2220
[42] Lazarus E.A. *et al* 1992 *Phys. Plasmas* B **4** 3644
[43] Gates D.A. *et al* 2006 *Phys. Plasmas* **13** 056122
[44] Gerhardt S.P. *et al* 2011 *Nucl. Fusion* **51** 073031
[45] Hofmann F., Dutch M.J., Ward D.J., Anton M., Furno I., Lister J.B. and Moret J.-M. 1997 *Nucl. Fusion* **37** 681
[46] Kessel C.E., Heitzenroeder P. and Jun C. 2001 *Nucl. Fusion* **41** 953
[47] Hofmann F., Favre A., Isoz P.-F., Martin Y., Moret J.-M. and Nieswand C. 2000 *Nucl. Fusion* **40** 767
[48] Humphreys D.A. *et al* 2009 *Nucl. Fusion* **49** 115003
[49] Hawryluk R.J. *et al* 2009 *Nucl. Fusion* **49** 065012
[50] Whyte D.G. *et al* 2002 *Phys. Rev. Lett.* **89** 055001
[51] Whyte D.G. *et al* 2003 *J. Nucl. Mater.* **313–316** 1239
[52] Granetz R., Whyte D.G., Izzo V.A., Biewer T., Reinke M.L., Terry J., Bader A., Bakhtiari M., Jernigan T. and Wurden G. 2006 *Nucl. Fusion* **46** 1001
[53] Granetz R.S. *et al* 2007 *Nucl. Fusion* **47** 1086
[54] Hollmann E.M. *et al* 2008 *Nucl. Fusion* **48** 115007
[55] Pautasso G. *et al* and the ASDEX Upgrade Team 2007 *Nucl. Fusion* **47** 900
[56] Pautasso G. *et al* and the ASDEX Upgrade Team 2009 *Plasma Phys. Control Fusion* **51** 124056
[57] Hollmann E.M. *et al* 2010 *Phys. Plasmas* **17** 056117
[58] Lehnen M. *et al* and JET EFDA contributors 2010 *Proc. 23rd Int. Conf. on Fusion Energy 2010 (Daejeon, South Korea 2010)* (Vienna: IAEA) CD-ROM file EXS/P2-13 and http://www-naweb.iaea.org/napc/physics/FEC/FEC2010/html/index.htm
[59] Bakhtiari M., Olynyk G., Granetz R., Whyte D.G., Reinke M.L., Zhurovich K. and Izzo V. 2011 *Nucl. Fusion* **51** 063007
[60] Sykes A. *et al*, 1999 *Nucl. Fusion* **39** 1271
[61] Edlington T., Martin R. and Pinfold T. 2001 *Rev. Sci. Instrum.* **72** 421
[62] Counsell G.F., Martin R., Pinfold T., Taylor D. and the MAST team 2007 *Plasma Phys. Control. Fusion* **49** 435
[63] Ono M. *et al* and the NSTX Team 2000 *Nucl. Fusion* **40** 557
[64] Peng Y.K.M. and Strickler D.J. 1986 *Nucl. Fusion* **26** 769
[65] Stambaugh R.D., Chan V.S., Miller R.L. and Schaffer M.J. 1998 *Fusion Technol.* **33** 1
[66] Miller R.L., Lin-Liu Y.R., Turnbull A.D., Chan V.S., Pearlstein L.D., Sauter O. and Villard L. 1997 *Phys. Plasmas* **4** 1062
[67] Menard J.E., Jardin S.C., Kaye S.M., Kessel C.E. and Manickam J. 1997 *Nucl. Fusion* **37** 595
[68] Wong C.P.C., Weslay J.C., Stambaugh R.D. and Cheng E.T. 2002 *Nucl. Fusion* **42** 547
[69] Lin-Liu Y.R. and Stambaugh R.D. 2004 *Nucl. Fusion* **44** 548
[70] Ferron J.R., Kellman A.G., McKee G.R., Osborne T.H., Petrach P., Taylor T.S. and Wight J. 1992 An advanced plasma control system for the DIII-D tokamak *Proc. 14th IEEE/NPSS Symp. on Fusion Engineering (San Diego, CA, 1992)* vol II (Piscataway, NJ: IEEE) p 761 http://ieeexplore.ieee.org/stamp/stamp.jsp?tp=&arnumber=218736
[71] Penaflor B.G., Ferron J.R. and Walker M.L. 1996 A structured architecture for advanced plasma control experiments *Proc. 19th Symp. on Fusion Technology (Lisbon, Portugal, 16–20 September)* p 965 http://www.osti.gov/bridge/servlets/purl/450046-Deomaq/webviewable/450046.pdf
[72] Penaflor B.G., Piglowski D.A., Ferron J.R. and Walker M.L. 2000 *IEEE Trans. Nucl. Sci.* **47** 201
[73] Gates D. *et al* 2006 *Fusion Eng. Des.* **81** 1911
[74] Mastrovito D., Gates D., Gerhardt S., Lawson J., Ludescher-Furth C. and Marsala R. 2010 *Fusion Eng. Des.* **85** 447
[75] Ferron J.R., Walker M.L., Lao L.L., St John H.E., Humphreys D.A. and Leuer J.A. 1998 *Nucl. Fusion* **38** 1055
[76] Gates D.A. *et al* 2006 *Nucl. Fusion* **46** 17
[77] Gerhardt S.P. *et al* 2009 *Nucl. Fusion* **49** 032003
[78] Sabbagh S.A. *et al* 2006 *Nucl. Fusion* **46** 635
[79] Sabbagh S.A. *et al* 2010 *Nucl. Fusion* **50** 025020
[80] Raman R. *et al* 2009 *Nucl. Fusion* **49** 095025
[81] Nelson B.A., Jarboe T.R., Mueller D., Raman R., Bell M., Menard J., Ono M., Roquemore A.L., Soukhanovskii V., Yuh H. and the NSTX Research Team 2011 *Nucl. Fusion* **51** 063008
[82] Gerhardt S.P., Fredrickson E., Guttadora L., Kaita R., Kugel H., Menard J. and Takahashi H. 2011 *Rev. Sci. Instrum.* **82** 103502
[83] Hutchinson I.H. 1987 *Principles of Plasma Diagnostics* (Cambridge: Cambridge University Press)
[84] Kugel H.W. *et al* 2009 *Fusion Eng. Des.* **84** 1125
[85] Sabbagh S.A. *et al* and NSTX Research Team 2001 *Nucl. Fusion* **41** 1601
[86] Menard J.E. *et al* 2006 *Phys. Rev. Lett* **97** 095002
[87] Gates D., Menard J.E. and Marsala R.J. 2004 *Rev. Sci. Instrum.* **75** 5090
[88] Kugel H.W. *et al* 2008 *Phys. Plasmas* **15** 056118
[89] Whyte D.G., Humphreys D.A. and Taylor P.L. 2000 *Phys. Plasmas* **7** 4057
[90] Gerasimov S.N., Hender T.C., Johnson M.F., Zakharov L.E. and the JET EFDA contributors 2010 Scaling JET Disruption Sideways Forces to ITER *37th European Physical Society Conf. on Plasma Physics (Dublin, Ireland, 2010)* paper P4.121 and http://ocs.ciemat.es/EPS2010PAP/pdf/P4.121.pdf
[91] Hender T.C. *et al* and JET-EFDA Contributors 2010 *Proc. 23rd Int. Conf. on Fusion Energy 2010 (Daejeon, South Korea 2010)* (Vienna: IAEA) CD-ROM file EXS/10-03 and http://www-naweb.iaea.org/napc/physics/FEC/FEC2010/html/index.htm